Precision Spectroscopy of Yb atoms and Design of linear ion trap for confining Yb ions

A Thesis

submitted to

Indian Institute of Science Education and Research Pune
in partial fulfillment of the requirements for the
Master of Science in Quantum Technology

by

Aniket Rohila

Indian Institute of Science Education and Research Pune

April, 2026

Supervisor: Dr. Subhasis Panja

Certificate

This is to certify that this dissertation entitled **"Precision Spectroscopy of Yb atoms and Design of linear ion trap for confining Yb ions"** submitted towards the partial fulfilment of the Master of Science in Quantum Technology represents study/work carried out by Aniket Rohila from Indian Institute of Science Education and Research Pune under the supervision of Dr. Subhasis Panja (Indian Standard Time (IST), Department of Metrology, CSIR - National Physics Laboratory, India) during the academic year 2025–2026.

Subhasis Panja

Signature of Supervisor (Dr. Subhasis Panja)

Date: 27-04-2026

Dr. SUBHASIS PANJA
Sr. Principal Scientist
CSIR - National Physical Laboratory
Dr. K.S. Krishnan Marg, New Delhi-110012

Declaration

I hereby declare that the matter embodied in the report entitled **"Precision Spectroscopy of Yb atoms and Design of linear ion trap for confining Yb ions"** are the results of the work carried out by me at the CSIR - National Physics Laboratory under the supervision of Dr. Subasish Panja (Indian Standard Time (IST) Department of Metrology CSIR - National Physics Laboratory, India) and the same has not been submitted elsewhere for any other degree.

Signature of the Author (Aniket Rohila) Date: 15/05/2026

Abstract

This thesis presents a study of two important areas of atomic and quantum technologies: precision spectroscopy of neutral Ytterbium (Yb) atoms and the simulation of ion confinement using radio-frequency ion traps. The work focuses on overcoming limitations associated with Doppler broadening in spectroscopy and static confinement of charged particles.

High-resolution spectroscopy of the $^1S_0 \rightarrow {}^1P_1$ transition of neutral Ytterbium at 398.911 nm was investigated using saturation absorption spectroscopy (SAS). Conventional absorption spectroscopy measurements produced Doppler-broadened Gaussian profiles originating from the thermal velocity distribution of atoms, limiting the ability to resolve fine spectral structures. To overcome this limitation, a pump–probe configuration employing counter-propagating laser beams was implemented to isolate atoms with nearly zero velocity along the laser propagation axis, enabling the observation of narrow Doppler-free spectral features. Measurements were performed at different pump powers to investigate the effect of power broadening and its influence on spectral linewidth. Although a fully resolved Lamb dip could not be conclusively obtained, the experimental setup was successfully developed and optimized, providing an important foundation for future precision measurements. In addition, a complete optical apparatus for Cross-Beam Saturated Absorption Spectroscopy (CBSAS) was designed and assembled to reduce power broadening effects and enable improved frequency measurements in future studies.

The second part of this work investigates ion confinement using radio-frequency quadrupole ion traps. Since stable three-dimensional confinement cannot be achieved using static electric fields due to the constraints imposed by Laplace's equation, dynamic confinement through time-varying fields was studied. The motion of trapped ions was analyzed through the Mathieu equations and simulated numerically using the Runge–Kutta method. Stable trapping conditions were examined for different stability parameters, and bounded ion trajectories were observed within specific stability regions. The simulations demonstrate the coexistence of slow secular motion and rapid micromotion in trapped-ion dynamics. The results also indicate that practical electrode geometries can achieve stable confinement despite deviations from ideal quadrupole fields.

Overall, this work establishes both an experimental and computational framework for future investigations in high-resolution spectroscopy and trapped-ion systems, with potential applications in atomic clocks, laser cooling, quantum information processing, and precision quantum technologies.

Acknowledgements

I would like to express my sincere gratitude to my supervisor, Dr. Subasish Panja, for providing me the opportunity to gain exposure in the Time and Frequency Standard Group at the Indian Standard Time (IST) Division, Department of Metrology, CSIR–National Physics Laboratory, India. During this period, I had the chance to explore experimental techniques such as Saturation Absorption Spectroscopy and simulation techniques such as the Runge–Kutta method. Through his consistent mentorship, guidance, and encouragement, I was motivated to expand my knowledge and continually challenge myself. I sincerely appreciate his role not only as a supervisor but also as a mentor whose constant encouragement and guidance have greatly influenced my learning process and helped me move forward with confidence throughout this journey.

I am equally grateful to Prof. Vishvendra S. Ponnia for giving me the opportunity to study Lindblad system dynamics at the Indian Institute of Technology Roorkee. This experience helped improve my understanding of open quantum system dynamics and significantly contributed to my academic growth. Beyond this, his guidance and valuable advice on what to pursue and what to avoid have been immensely helpful in shaping my academic perspective and decision-making. I am also sincerely thankful for his continuous support and mentorship, as he has guided me as a mentor throughout my academic journey and continues to do so even today.

I would also like to express my sincere gratitude to my thesis expert, Prof. Umakant D. Rapol, for giving me my first research project and providing me with the opportunity to explore quantum technologies through a project on the simulation of ion trap geometry during the winter of 2024. This experience played an important role in building my confidence in research and helped me discover and develop my interest in ion trap systems. I am especially thankful for his continuous support and guidance, and for later contributing as my thesis expert, which further enriched my academic journey.

I am sincerely thankful to the Head of the Department, Prof. T. S. Mahesh, and the MSc Coordinator, Prof. Sreejith G. J., for providing the necessary facilities and creating a supportive academic environment.

My heartfelt thanks go to the members of the IST Lab, especially Pallab Roy,

Sourin Choudhary, and the rest of the group, for their valuable suggestions and continuous guidance in both theoretical understanding and experimental techniques, which were essential for the development of the experimental setup.

I would also like to express my sincere gratitude to all my batchmates — Sayantan, Nikhil, Chandan, Shreyash, Vikash, and Deepanshu — for their constant motivation, support, and camaraderie, which made my academic journey a memorable and enriching experience.

I am forever indebted to my parents and my brother for their unwavering support, endless faith, and unconditional love, which have been my greatest source of strength throughout my journey.

Last but not least, I would like to express my sincere gratitude to everyone whom I may have unintentionally missed acknowledging, for their support, encouragement, and contributions that have inspired me and strengthened my belief that my work will continue to flourish.

Contents

List of Figures

Chapter 1

Precision Spectroscopy

1.1 Introduction

1.1.1 Role of Spectroscopy in Atomic Physics

Spectroscopy plays a fundamental role in our understanding of atomic physics, providing precise measurements of transition frequencies, natural linewidths, and interaction dynamics that form the experimental foundation of modern quantum mechanics [2]. Beyond fundamental science, spectroscopic techniques are central to a wide range of high-resolution applications, including the cooling and trapping of neutral atoms and ions, optical atomic clocks, and tests of fundamental symmetry laws.

Traditionally, optical spectroscopy was performed by dispersing the light emitted by excited matter, or by analysing the light transmitted through an absorbing medium. The development of tunable monochromatic laser sources transformed this field, enabling spectra to be recorded one wavelength at a time by measuring the transmitted or fluorescence intensity as a function of laser frequency. This approach offers dramatically higher spectral brightness and resolution compared to broadband lamp sources, and has become the standard method for precision atomic spectroscopy.

However, a fundamental limitation arises from the thermal motion of atoms in a gas or atomic beam. Because atoms move at a distribution of velocities, each atom experiences a slightly different Doppler shift of the laser frequency in its rest frame. As a result, different velocity classes of atoms absorb light at slightly different frequencies, and the observed absorption profile is broadened into a Gaussian envelope [3]. This *Doppler broadening* typically amounts to several hundred megahertz at room temperature, completely obscuring fine spectral structures such as hyperfine splittings and isotope shifts, which can be as small as a few tens of megahertz or less. Overcoming this limitation is the central challenge of high-resolution optical spectroscopy.

1.1.2 Doppler-Free Spectroscopy and the SAS Technique

Several techniques have been developed to suppress Doppler broadening and recover the intrinsic spectral resolution set by the natural linewidth of the atomic transition. Among these, *saturated absorption spectroscopy* (SAS) is one of the most widely used and experimentally accessible methods [4]. In SAS, a strong pump beam and a weak probe beam counter-propagate through the atomic medium. At the exact atomic transition frequency, both beams interact with the same zero-velocity atoms, producing a narrow Doppler-free transmission peak known as a *Lamb dip* at the centre of the broad absorption profile [2]. The theoretical foundations of SAS are discussed in detail in Section 1.2.5. The importance of these Doppler-free techniques is reflected in three Nobel Prizes in Physics: in 1981 for laser spectroscopy, in 1997 for laser cooling and trapping, and in 2001 for Bose–Einstein condensation [5].

1.1.3 Limitations of Conventional SAS and the Cross-Beam Approach

A well-known limitation of conventional SAS is *power broadening*: at high pump intensities, the Lamb dip linewidth increases with laser power, degrading spectral resolution. To overcome this, an alternative geometry known as *cross-beam saturated absorption spectroscopy* (CBSAS) has been explored [1], in which the pump and probe beams intersect orthogonally rather than counter-propagating along the same axis. This orthogonal geometry reduces the sensitivity of the spectral features to laser power, making CBSAS better suited for precision frequency measurements. The detailed theoretical comparison between SAS and CBSAS, including the inherent frequency shift introduced by the orthogonal geometry, is presented in Section 1.2.6.

1.1.4 Ytterbium as a Model System

In this work, we study the ${}^1S_0 \rightarrow {}^1P_1$ transition of neutral Ytterbium at 398.911 nm. Ytterbium is particularly well suited for precision spectroscopy due to its seven stable isotopes, including two fermionic isotopes with non-zero nuclear spin that exhibit hyperfine structure. These hyperfine splittings are unresolvable with Doppler-limited spectroscopy and provide a direct motivation for implementing Doppler-free techniques. A detailed description of the relevant Ytterbium energy levels and isotopic structure is given in Section 1.2.2.

1.1.5 Scope and Structure of This Thesis

This thesis describes the design, construction, and initial operation of a laser spectroscopy apparatus for Doppler-free spectroscopic studies of the $^1S_0 \rightarrow {}^1P_1$ transition of neutral Ytterbium. The work was carried out over a period of three months and encompasses conventional absorption spectroscopy, saturation absorption spectroscopy at multiple pump power levels, and the commissioning of the complete optical apparatus for cross-beam saturated absorption spectroscopy.

The remainder of this chapter is organised as follows. Section 1.2 provides the theoretical background, covering Doppler broadening, the Beer–Lambert law, and the principles of saturation absorption spectroscopy. Section 1.3 describes the experimental apparatus in detail, including the laser system, beam preparation optics, atomic beam source, detection system, and Fabry–Perot interferometer. Section 1.4 presents and discusses the experimental results. Section 1.5 summarises the conclusions of the work, and Section 1.6 outlines the future experimental programme including planned CBSAS measurements and hyperfine structure studies.

1.2 Background

1.2.1 Spectral Line Broadening

Spectral lines in atomic spectra are never perfectly sharp; they always possess a finite width arising from one or more physical broadening mechanisms. Understanding these mechanisms is essential for interpreting experimental spectra and for identifying the techniques needed to achieve high spectral resolution.

The most fundamental source of linewidth is the *natural linewidth*, which arises from the finite lifetime of the excited atomic state due to spontaneous emission. By the energy–time uncertainty principle, an excited state with lifetime τ has an energy uncertainty $\Delta E \sim \hbar/\tau$, which translates into a Lorentzian lineshape with a full width at half maximum (FWHM) given by

$$\Gamma = \frac{1}{\tau}. \tag{1.1}$$

The natural linewidth is the same for all atoms of the same species regardless of their velocity or environment, and therefore represents a *homogeneous* broadening mechanism. For the ${}^1S_0 \rightarrow {}^1P_1$ transition of Ytterbium at 398.911 nm, the natural linewidth is approximately $\Gamma/2\pi \approx 28\,\mathrm{MHz}$.

In contrast, *Doppler broadening* is an *inhomogeneous* broadening mechanism: different atoms contribute to the absorption at different frequencies depending on their individual velocities. Since atoms in a thermal gas follow a Maxwell–Boltzmann velocity distribution, the resulting lineshape is a Gaussian rather than a Lorentzian, and its width is typically much larger than the natural linewidth at room temperature. In the absence of Doppler broadening, the achievable spectral resolution can reach 10^8–10^9, allowing very fine spectral features to be resolved. However, at room temperature, Doppler broadening typically reduces the effective resolution to approximately 10^6, a loss of nearly three orders of magnitude [4].

1.2.2 Ytterbium Atom

Ytterbium is a rare-earth element with atomic number $Z = 70$ belonging to the lanthanide series. Its ground state electronic configuration is $[\mathrm{Xe}]\,4f^{14}6s^2$, giving a ${}^1S_0$ ground state with zero total angular momentum. This closed-shell ground state is particularly advantageous for laser cooling and precision spectroscopy because it eliminates complications from ground-state magnetic substructure.

Ytterbium has seven stable isotopes with the following natural abundances: ^{168}Yb (0.13%), ^{170}Yb (3.04%), ^{171}Yb (14.28%), ^{172}Yb (21.83%), ^{173}Yb (16.13%), ^{174}Yb (31.83%), and ^{176}Yb (12.76%). The even isotopes (^{168,170,172,174,176}Yb) have zero nu-

clear spin and therefore no hyperfine structure, while the odd isotopes (^{171}Yb with $I = 1/2$ and ^{173}Yb with $I = 5/2$) exhibit hyperfine splitting of their excited states.

The spectroscopic transitions of neutral Ytterbium relevant to this work are:

- **Target transition:** $^1S_0 \rightarrow {}^1P_1$ at 398.911 nm (natural linewidth $\Gamma/2\pi \approx 28$ MHz). This strong, dipole-allowed transition is used in this experiment for absorption and saturation spectroscopy, and is commonly employed for Zeeman slowing and first-stage laser cooling.
- **Intercombination transition:** $^1S_0 \rightarrow {}^3P_1$ at 556 nm (natural linewidth $\Gamma/2\pi \approx 182$ kHz). This narrow transition is used for second-stage laser cooling to sub-microkelvin temperatures.

1.2.3 Doppler Broadening

An atom at rest in the laboratory frame has a natural transition frequency ω_0. When the atom moves with velocity v relative to the laboratory frame, the frequency of the incident radiation as seen by the atom is Doppler shifted. The observed angular frequency in the atom's rest frame is

$$\omega' = \omega - \mathbf{k} \cdot \mathbf{v}, \tag{1.2}$$

where $\mathbf{k}$ is the wavevector of the radiation. Only the component of velocity along the beam propagation direction contributes to the Doppler shift. Taking both $\mathbf{k}$ and $\mathbf{v}$ along the z-axis, the resonance condition $\omega' = \omega_0$ gives a detuning

$$\delta \equiv \omega' - \omega_0 = kv = \frac{\omega_0 v}{c}. \tag{1.3}$$

This shows that atoms with different velocities interact with different laser frequencies, directly leading to Doppler broadening.

In thermal equilibrium, atomic velocities follow the Maxwell–Boltzmann distribution:

$$f(v)\,\mathrm{d}v = \frac{1}{u\sqrt{\pi}} \exp\left(-\frac{v^2}{u^2}\right) \mathrm{d}v, \tag{1.4}$$

where $u = \sqrt{2k_B T/M}$ is the most probable speed, k_B is the Boltzmann constant, T is the temperature, and M is the atomic mass. Transforming the velocity distribution into a frequency distribution, the Doppler-broadened lineshape is a Gaussian:

$$g_D(\omega) = \frac{c}{u\omega_0\sqrt{\pi}} \exp\left[-\frac{c^2}{u^2}\left(\frac{\omega - \omega_0}{\omega_0}\right)^2\right]. \tag{1.5}$$

The FWHM of this Gaussian profile is

$$\Delta\omega_D = \frac{2\omega_0}{c}\sqrt{\ln 2}\sqrt{\frac{2k_BT}{M}}, \tag{1.6}$$

showing that the Doppler width scales as $\Delta\omega_D \propto \sqrt{T/M}$: it increases with temperature and decreases with atomic mass.

1.2.4 Absorption Spectroscopy

When a monochromatic beam of intensity I_0 propagates through an atomic medium of length L, the transmitted intensity I is attenuated by absorption according to the Beer–Lambert law:

$$I = I_0 \exp[-\alpha(\omega)L], \tag{1.7}$$

where $\alpha(\omega)$ is the frequency-dependent absorption coefficient. In a thermal atomic beam, the absorption coefficient is proportional to the number density of atoms and their velocity distribution, and the resulting absorption profile inherits the Gaussian lineshape of the Doppler-broadened velocity distribution. The transmittance $T = I/I_0$ and absorbance $A = -\log_{10} T$ are the standard measurable quantities in absorption spectroscopy.

Doppler-broadened absorption spectroscopy is a straightforward and robust technique for locating atomic transitions and measuring coarse spectral features such as the isotope structure of Ytterbium. However, its resolution is fundamentally limited by the Doppler width, and fine structures such as hyperfine splittings of the excited state cannot be resolved without Doppler-free methods.

1.2.5 Saturation Absorption Spectroscopy

Saturation absorption spectroscopy overcomes the Doppler limit by using two counter-propagating beams from the same laser source: a strong *pump* beam and a weak *probe* beam. Consider the pump beam propagating in the $+z$ direction and the probe beam in the $-z$ direction. An atom moving with velocity v_z along the z-axis sees the pump beam at frequency $\omega(1 - v_z/c)$ and the probe beam at frequency $\omega(1 + v_z/c)$. For the pump to be resonant with the atom, $\omega(1 - v_z/c) = \omega_0$, giving $v_z = c(1 - \omega_0/\omega)$. For the probe to be resonant, $v_z = -c(1 - \omega_0/\omega)$. The only velocity class for which both conditions are simultaneously satisfied is $v_z = 0$, and this occurs precisely when $\omega = \omega_0$.

At this laser frequency, the pump beam saturates the $v_z = 0$ atoms, depleting the ground-state population and reducing their absorption cross-section. The probe beam, which also interacts with this same velocity class at $\omega = \omega_0$, experiences re-

duced absorption as a result. This produces a narrow *Lamb dip* at the centre of the Doppler-broadened probe absorption profile, with a linewidth approaching the natural linewidth Γ [2].

At high laser intensities, however, power broadening increases the effective linewidth of the Lamb dip:

$$\Gamma_{\text{eff}} = \Gamma\sqrt{1+s}, \qquad s = \frac{I}{I_s}, \tag{1.8}$$

where the saturation intensity is

$$I_s = \frac{\pi hc\Gamma}{3\lambda^3}. \tag{1.9}$$

This power broadening imposes a trade-off between signal strength and spectral resolution in conventional SAS.

1.2.6 Cross-Beam Saturated Absorption Spectroscopy

In cross-beam saturated absorption spectroscopy (CBSAS), the pump and probe beams are arranged to intersect orthogonally rather than propagating along the same axis in opposite directions [6]. In this geometry, the pump beam propagates along one axis (say z) and the probe beam propagates along an orthogonal axis (say x). The pump beam selects atoms based on their z-velocity component, while the probe beam interrogates atoms based on their x-velocity component. Since these are independent degrees of freedom in the thermal velocity distribution, the velocity class overlap between pump and probe is greatly reduced compared to the counter-propagating case.

As a result, the pump beam does not as efficiently saturate the specific velocity class probed by the probe beam, and the saturation signal is less sensitive to the pump intensity. Spectral features obtained with CBSAS therefore exhibit reduced power broadening, making the technique better suited for precision linewidth measurements where the laser power cannot easily be stabilised to the sub-percent level required by conventional SAS.

It must be emphasised, however, that the orthogonal geometry modifies the resonance condition. The frequency at which the CBSAS feature appears is shifted from the bare transition frequency ω_0 by an amount that depends on the geometry and the velocity distribution of the atomic beam. Quantitative frequency measurements with CBSAS therefore require a calibrated SAS reference to determine the magnitude of this shift. For this reason, successful operation of SAS is a necessary prerequisite before meaningful CBSAS measurements can be performed.

1.3 Experimental Setup

Figure 1.1 is a schematic diagram of a laser spectrometer based on a tunable diode laser like that described in Ref. [1]. The experimental setup for saturation absorption spectroscopy (SAS) is designed to eliminate Doppler broadening and enable high-resolution measurement of atomic transitions. The laser frequency can be swept through the atomic absorption lines by varying the voltage across a piezoelectric transducer (PZT) to change the length of the laser cavity [2]. The 399 nm wavelength beam from the laser is divided into two beams: the most intense beam, referred to as the *pump* beam, and the other beam, which is of considerably lower intensity, referred to as the *probe* beam. The probe beam is sent through the atomic medium in the direction counter-propagating to that of the pump beam and is detected by a photodiode. Both beams interact with the same group of atoms — those with zero velocity along the laser axis — to produce Doppler-free spectral features.

We also send a reference probe beam parallel to the overlap probe beam, which does not interact with the pump beam. The signals produced by the two probe beams at the photodiodes are adjusted to be equal and then subtracted from each other. It is the difference between the two signals that is recorded as the final experimental signal.

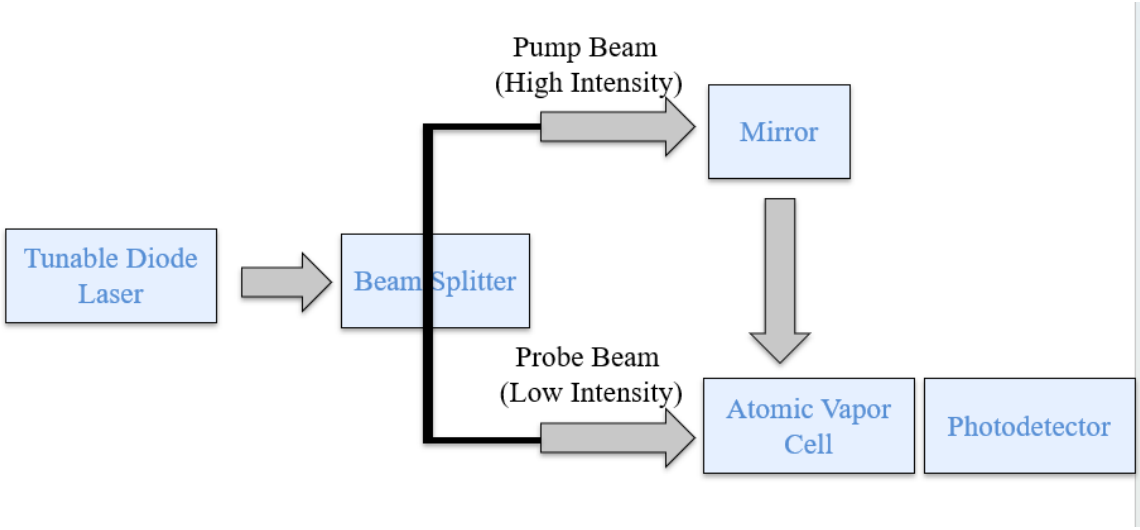

Figure 1.1: Schematic representation of the SAS experimental setup, showing the tunable diode laser, beam splitter, pump and probe beam paths, atomic vapour cell, and photodetector.

A schematic representation typically includes:

- Tunable diode laser
- Beam splitter to generate pump and probe beams
- Mirrors for beam alignment

- Atomic vapour cell or atomic beam source
- Photodetector for signal acquisition

The laser frequency is scanned across the atomic transition, and the transmitted probe intensity is recorded as a function of frequency.

1.3.1 Laser System

A narrow-linewidth tunable diode laser is used as the light source. In this experiment, an external cavity diode laser (ECDL) operating at the relevant atomic transition wavelength of 398.911 nm for Ytterbium is employed. The laser provides:

- High spectral resolution with a linewidth of $\sim$1 MHz or below
- Continuous tunability over several gigahertz
- Stable single-mode operation

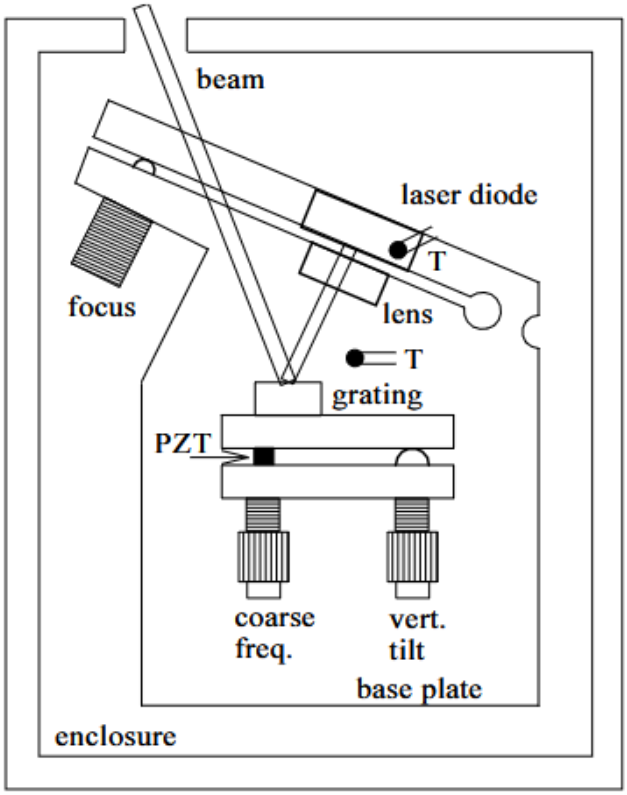

Figure 1.2: Schematic of the external cavity diode laser used in this experiment [1], showing the laser diode, collimating lens, diffraction grating, PZT actuator, and frequency adjustment components.

The laser frequency is scanned using a piezoelectric actuator or current modulation. This scanning allows the observation of both Doppler-broadened and Doppler-free

spectral features. The laser frequency can be adjusted through several parameters: laser temperature, laser current, and the position and orientation of the piezoelectric grating. The laser temperature and current provide coarse tuning over a wide frequency range, while fine tuning is achieved by adjusting the grating position using the piezoelectric transducer (PZT).

The following safety procedures must be followed at all times [1]:

1. The diode laser used in this experiment has sufficient intensity to permanently damage the eye. Laser safety goggles must be worn when working on this experiment.

2. All reflective objects must be removed from the person, and all stray reflections from the experiment must be identified and blocked.

3. The PZT changes the cavity length, causing the laser frequency to vary continuously. If the cavity length changes too much, sudden frequency jumps (mode hops) occur. Careful optimisation of temperature and current allows continuous tuning without mode hopping.

4. The laser beam initially has an elliptical profile, which is converted into a circular beam using an anamorphic prism pair, while lenses can further adjust the beam diameter.

1.3.2 Beam Preparation and Splitting

The output beam from the laser is first passed through an optical isolator to prevent feedback into the laser cavity. It is then split into two beams using a beam splitter:

- **Pump beam:** High-intensity beam used to saturate the atomic transition.
- **Probe beam:** Low-intensity beam used to measure absorption.

Neutral density filters or polarising beam splitters are used to control the intensity ratio between the pump and probe beams. Waveplates (half-wave and quarter-wave plates) are used to adjust the polarisation, which is important for controlling selection rules and optimising the interaction with atomic transitions.

1.3.3 Atomic Medium

The atomic medium can be either a vapour cell or an atomic beam. In more advanced setups, an atomic beam is generated using an effusive oven. The oven is resistively heated to produce a collimated beam of atoms. The temperature of the oven determines the velocity distribution of atoms and hence the Doppler width.

The atomic beam propagates in a well-defined direction, typically perpendicular to the laser beams. This geometry reduces Doppler effects along certain directions. Atomic beams emerging from an oven have a distribution of velocities governed by thermal equilibrium, and their interaction with laser beams leads to Doppler-broadened spectra as described in Section 1.2.4.

1.3.4 Pump–Probe Geometry and Optical Alignment

Conventional SAS Geometry

The defining feature of SAS is the use of two counter-propagating beams. The pump and probe beams are aligned such that they overlap spatially within the atomic medium but propagate in opposite directions. The pump beam travels in one direction with high intensity, and the probe beam travels in the opposite direction with lower intensity.

Atoms with zero velocity component along the laser direction interact with both pump and probe beams at the same frequency, as they experience no Doppler shift. In contrast, atoms with non-zero velocities see different frequencies for the two beams and do not contribute to simultaneous resonance. The pump beam saturates the transition for the zero-velocity atoms, leading to reduced absorption of the probe beam and producing a narrow Doppler-free feature.

Precise alignment of optical components is critical for successful SAS measurements. The pump and probe beams must:

- Overlap spatially within the atomic medium
- Be perfectly counter-propagating
- Maintain stable polarisation

Mirrors mounted on adjustable mounts are used to align the beams. Beam profiling tools or IR cards are often used to ensure proper overlap. In some setups, retroreflection is used, where the probe beam is reflected back along the same path to act as the pump beam.

Cross-Beam SAS Geometry

In the CBSAS configuration, shown in Figure 1.3, the pump and probe beams intersect orthogonally inside the vacuum chamber rather than counter-propagating along the same axis. As discussed in Section 1.2.6, this orthogonal geometry reduces the overlap of the velocity classes addressed by the pump and probe beams, resulting in spectral features with a weaker dependence on laser power compared to conventional SAS.

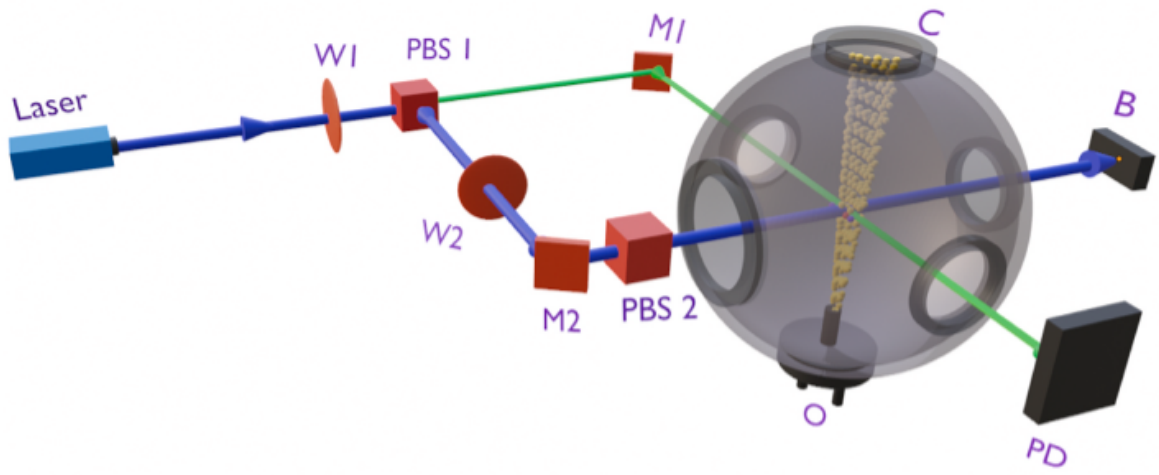

Figure 1.3: Experimental setup for recording Cross-Beam Saturated Absorption Spectra (CBSAS) of Yb atoms with orthogonal configuration of pump and probe laser beams. W1 and W2 are zero-order half-waveplates, PBS1 and PBS2 are polarising beam splitters, M1 and M2 are reflecting mirrors, PD is the photodiode, C is the vacuum chamber, and O is the atomic oven. The solid green line represents the probe beam and the blue line represents the pump beam.

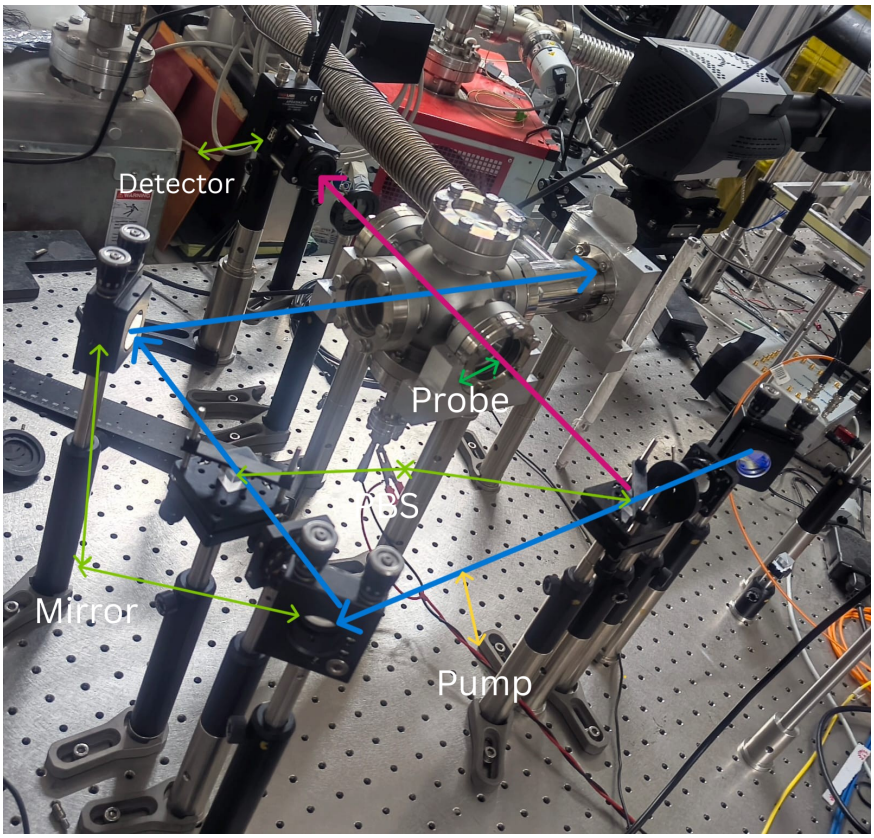

Figure 1.4: Photograph of the experimental setup on the optical table, with beam paths indicated.

It is important to note that the orthogonal geometry introduces an inherent frequency shift of the observed resonance relative to the bare atomic transition frequency. A well-resolved conventional SAS signal is therefore a necessary prerequisite before CBSAS measurements can be quantitatively interpreted. The complete CBSAS optical apparatus was assembled and aligned during this project, and is ready for use once the SAS signal has been optimised.

1.3.5 Detection System

The transmitted probe beam is detected using a photodiode. The detector converts optical intensity into an electrical signal, which is recorded as a function of laser frequency. To improve signal quality:

- Balanced photodetection may be used to reduce common-mode laser intensity noise
- Lock-in amplification can enhance the signal-to-noise ratio

The detected signal shows a Doppler-broadened absorption profile with narrow dips corresponding to Doppler-free resonances when the SAS conditions are met.

1.3.6 Fabry–Perot Interferometer

Once the laser temperature has stabilised and a laser current has been set, a voltage ramp is applied to the PZT, causing the laser frequency to smoothly sweep over several resonance frequencies of the Ytterbium atoms. The laser frequency during the sweep is monitored using a confocal Fabry–Perot interferometer.

The Fabry–Perot consists of two partially transmitting, identically curved mirrors separated by their radius of curvature. With the laser well aligned into the Fabry–Perot cavity, the transmitted intensity through the cavity becomes a periodic function of the laser frequency. The Fabry–Perot only transmits the laser beam at a set of discrete frequencies separated by the free spectral range (FSR):

$$\mathrm{FSR} = \frac{c}{4L}, \tag{1.10}$$

where L is the distance between the mirrors.

Consequently, as the frequency of the laser beam entering the cavity is swept, the transmission monitored by a photodetector on the other side of the cavity shows a series of peaks separated by the FSR. These peaks, or fringes, are monitored simultaneously with the absorption through the Ytterbium vapour and serve as frequency markers for tracking how the laser frequency changes during the sweep.

Figure 1.5: Photographs of the assembled experimental apparatus from multiple angles, showing the vacuum chamber, optical mounts, mirror alignment stages, and detector assembly.

1.3.7 Experimental Considerations

Several practical factors influence the quality of SAS measurements:

- **Laser intensity:** Higher intensity improves the signal amplitude, but causes power broadening of the Lamb dip, reducing spectral resolution.
- **Beam alignment:** Misalignment of the counter-propagating beams reduces the Doppler-free signal amplitude.
- **Temperature:** The oven temperature affects atomic density and Doppler width; higher temperatures increase flux but broaden the spectrum.
- **Stray reflections:** Reflections from optical surfaces such as vacuum chamber viewports can introduce spurious fringes that obscure the true spectral features.
- **Magnetic fields:** Stray magnetic fields can shift energy levels through the Zeeman effect, modifying the observed spectrum.

Careful optimisation of all these parameters is required to achieve high-resolution spectra.

1.4 Results and Discussion

In this work, absorption spectroscopy and saturation absorption spectroscopy (SAS) were performed on the $^1S_0 \rightarrow {}^1P_1$ transition of neutral Ytterbium at 398.911 nm. The primary objectives were to observe the Doppler-broadened absorption spectra, attempt to resolve Doppler-free features using SAS, and try to modify the experimental apparatus for cross-beam saturated absorption spectroscopy (CBSAS).

1.4.1 Doppler-Broadened Absorption Spectroscopy

The first set of measurements was performed using a single probe beam With the pump beam blocking and passing through the Ytterbium atomic beam. Only the reference probe beam reached the photodiode and we are getting a pure absorption signal. The recorded spectrum, shown in Figure 1.7, displays a broad Gaussian profile from the thermal velocity distribution of the atoms, described by the Maxwell–Boltzmann distribution with matching the theoretical prediction for Doppler broadening, as discussed in Section 1.2.2. The shape arises

Multiple resonance dips on the broad envelope arise from different isotopes and transitions of ytterbium. Their presence confirms correct laser tuning and proper functioning of the atomic beam. The recorded spectrum has noticeable noise, which may originate from several sources like laser intensity fluctuations during the frequency

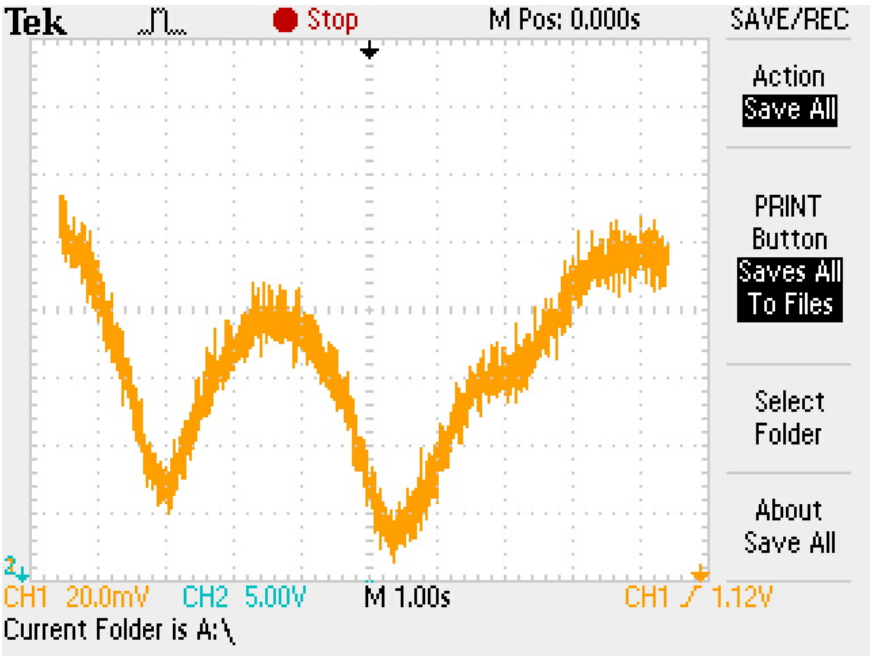

Figure 1.6: oscilloscope screenshot for Absorption spectra

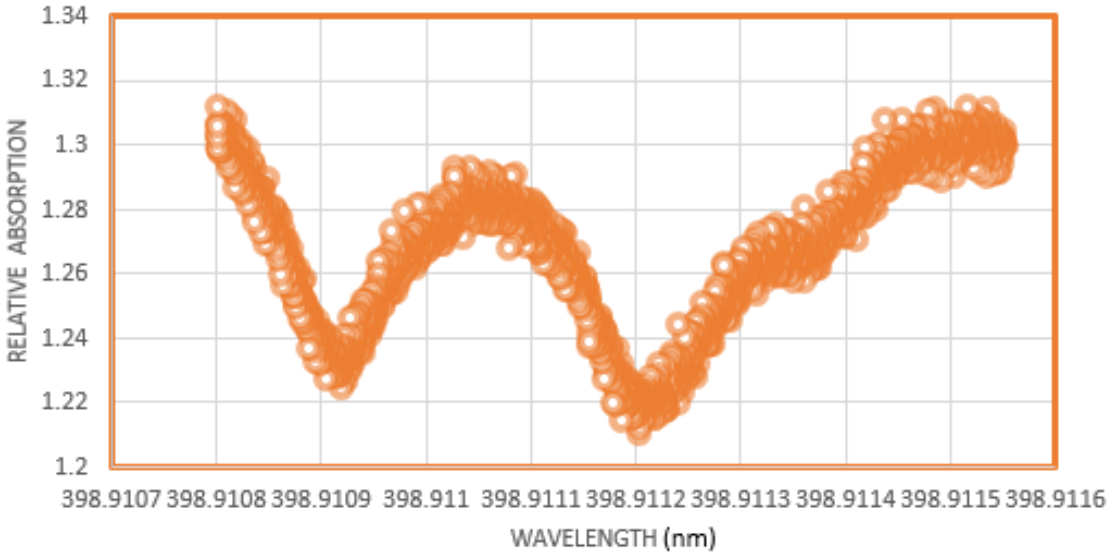

Figure 1.7: Absorption Spectra

sweep, scan nonlinearity of the piezoelectric transducer (PZT), detector noise in the photodiode circuit, and residual mechanical vibrations on the optical table. Despite these limitations, the Doppler-broadened absorption profile is clearly observed and qualitatively matches the expected thermal atomic beam lineshape.

1.4.2 Saturation Absorption Spectroscopy

Following the successful observation of the Doppler-broadened profile, the pump beam was introduced in the counter-propagating configuration to perform saturation absorption spectroscopy. Measurements were recorded at different pump power levels: 0.95 mW, 1.15 mW, and 1.37 mW, as shown in Figures 1.8, 1.11, and 1.10 respectively.

In each measurement, the SAS signal (probe beam with pump beam) was recorded simultaneously with the absorption reference signal (probe beam without pump) and difference between the two signals isolates the saturation contribution and reveals any Doppler-free features.

Upon subtracting the absorption background, a small residual feature is observed near 398.9114 nm in the 1.15 mW measurement (Figure 1.9) and a Lorentzian profile was fitted to this residual which indicates a narrow feature at approximately this wavelength. However, it must be noted that this feature sits close to the noise floor of the measurement, and its amplitude is comparable to the residual noise level after background subtraction.

Critically, when comparing results across different pump power levels, the position and amplitude of the observed feature do not show consistent and systematic behaviour expected from a well-resolved Lamb dip. A genuine Lamb dip should appear at a fixed transition frequency independent of pump power, and its linewidth should broaden systematically with increasing pump intensity according to the power-broadening relation:

$$\Gamma_{\text{eff}} = \Gamma\sqrt{1+s}, \tag{1.11}$$

where $s = I/I_s$ is the saturation parameter. While a hint of a feature is present in some traces, the lack of clear reproducibility across all pump power settings means that a definitive, well-resolved Doppler-free Lamb dip cannot be claimed from the present data.

The most likely contributing factors to the absence of a clearly resolved Lamb dip include the following. First, insufficient signal-to-noise ratio: the SAS signal is a small differential signal on top of a large background, and the present detection scheme may not have sufficient sensitivity to resolve it cleanly. Second, beam alignment sensitivity: even small deviations from perfect counter-propagation between the pump and probe beams can wash out the Lamb dip, as it relies on selecting atoms with strictly zero velocity along the beam axis. Third, optical feedback and stray reflections: any

residual reflections from optical surfaces, including the vacuum chamber windows, can introduce spurious interference fringes that obscure the true spectral features. Fourth, power broadening at higher intensities may have partially washed out the narrow feature at the higher pump powers used. Identifying and eliminating these noise sources is the primary requirement for future measurements.

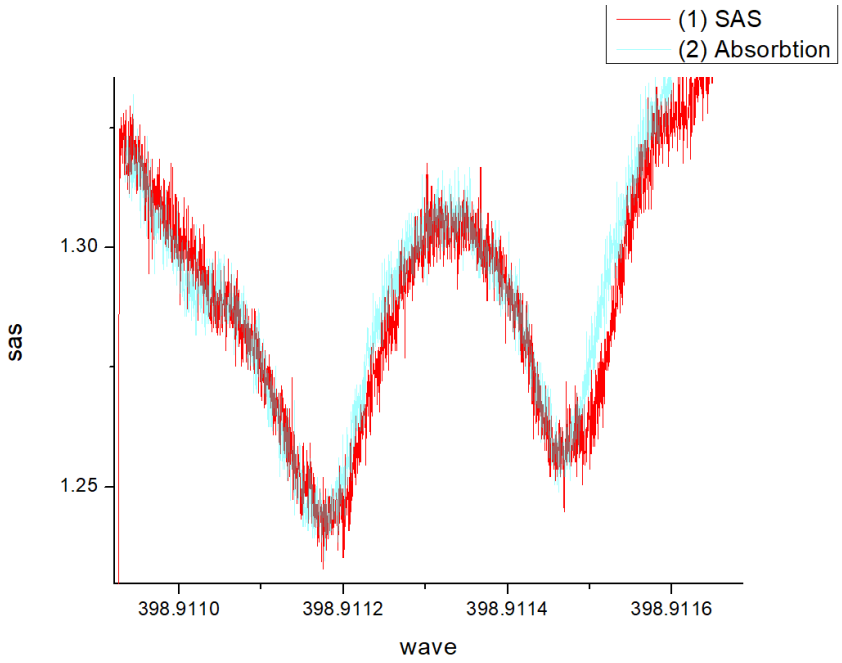

Figure 1.8: Pump Power- 1.15mW

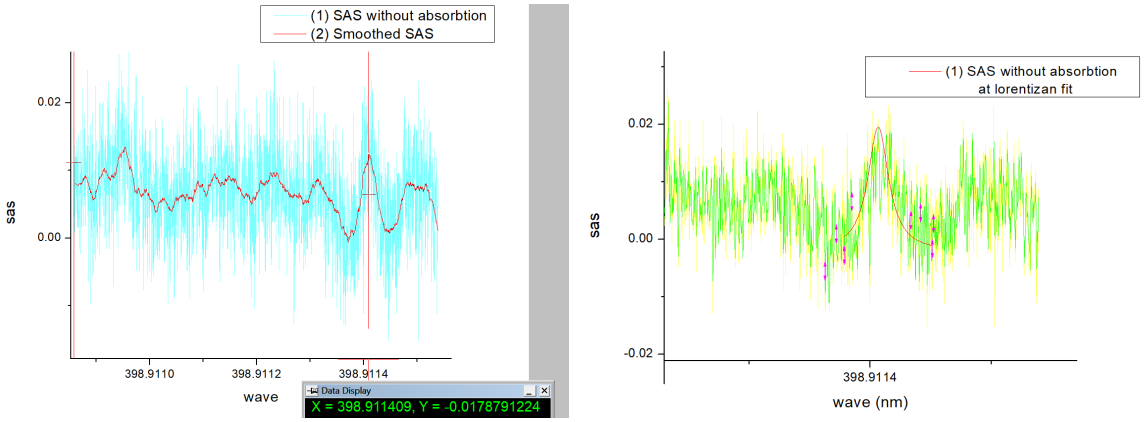

Figure 1.9: Pump Power- 1.15mW

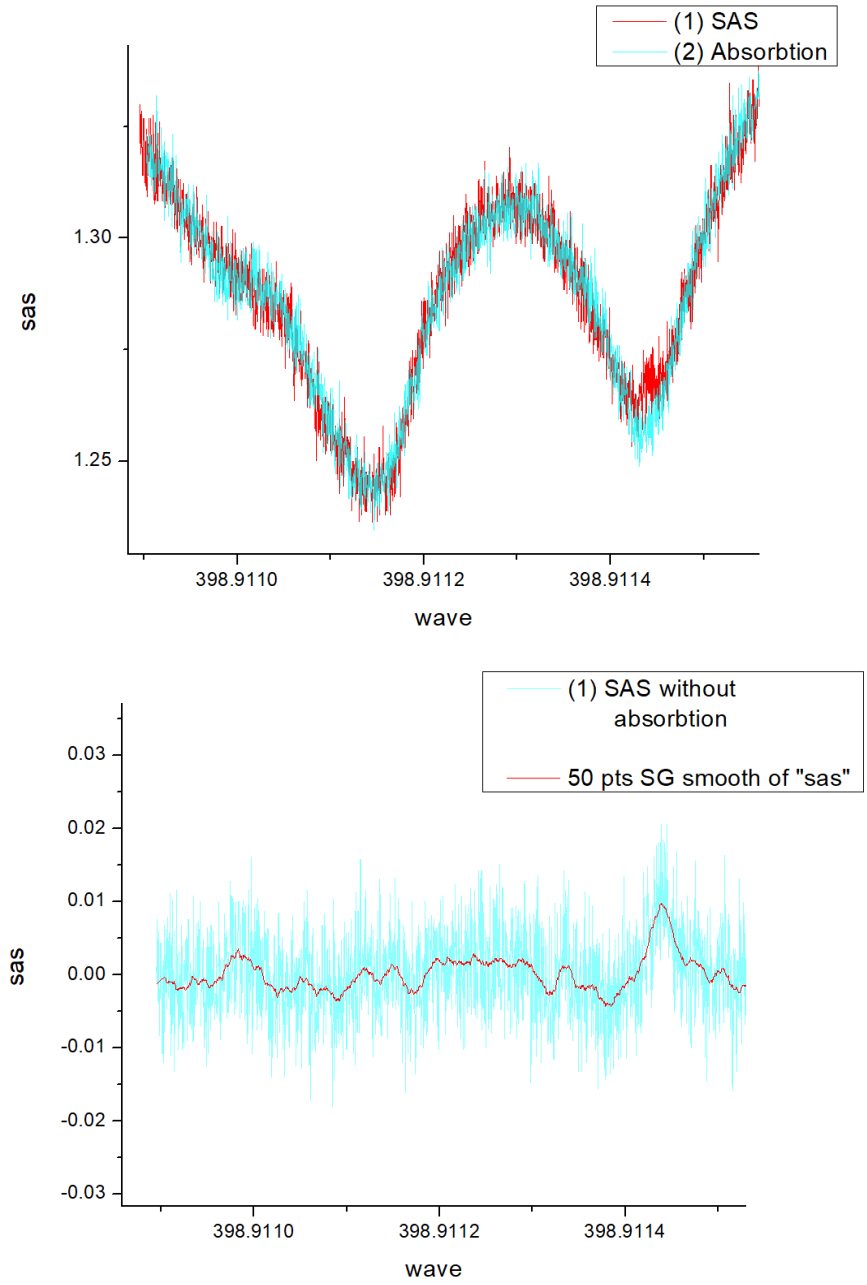

Figure 1.10: Pump Power - 1.37mW

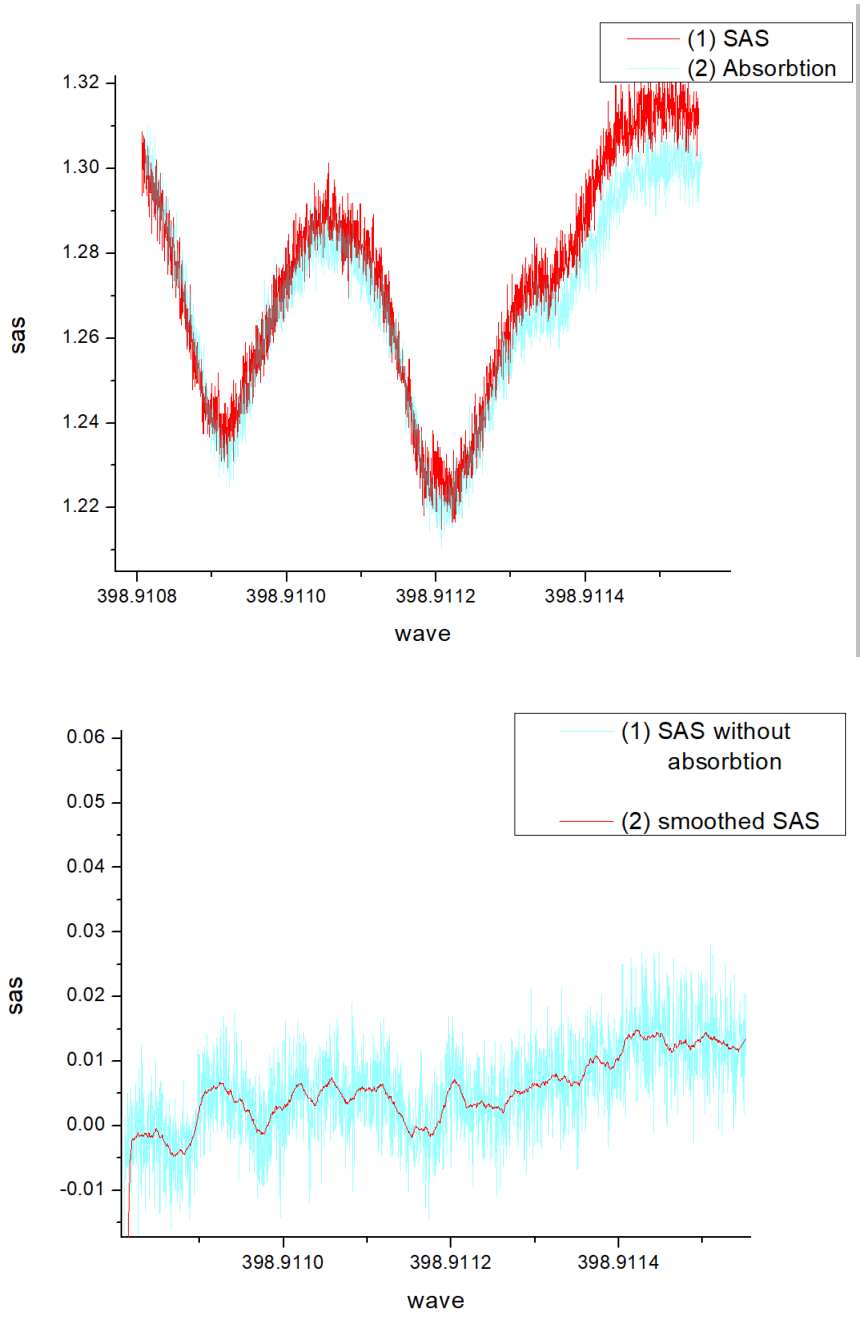

Figure 1.11: Pump Power - 0.95mW

1.4.3 Commissioning of the Cross-Beam SAS Apparatus

In parallel with the SAS measurements, the complete optical setup for cross-beam saturated absorption spectroscopy (CBSAS) was designed, assembled, and optically aligned. As described in Section 1.3.4, this configuration uses pump and probe beams oriented orthogonally rather than counter-propagating. The setup includes two zero-order half-waveplates (W1, W2), two polarising beam splitters (PBS1, PBS2), two mirrors (M1, M2), the vacuum chamber with the atomic oven, and the photodiode detector, as illustrated in Figure 1.1.

It is important that the CBSAS geometry introduces an inherent frequency shift in the observed spectral features relative to conventional SAS. In the counter-propagating SAS geometry, the Lamb dip appears precisely at the atomic transition frequency ω_0 because atoms with zero velocity component along the beam axis interact with both beams at the same frequency. In the orthogonal CBSAS geometry, the pump and probe beams address velocity components at small area i.e. unsaturated atoms numbers are decreased . This modifies the resonance condition and can result in a shift of the observed feature from the bare transition frequency. Consequently, a well-resolved and calibrated SAS signal is a necessary prerequisite for CBSAS, as it provides the absolute frequency reference against which any CBSAS shift can be measured and interpreted.

Since the SAS signal could not be fully resolved in the present work, proceeding to quantitative CBSAS measurements was not feasible within the scope of this project. Attempting to interpret CBSAS signals without a clean SAS reference would make any frequency shift measurement unreliable. The construction and alignment of the CBSAS apparatus nonetheless represents a significant step towards future measurements, and the optical setup is ready for use once the SAS signal is optimised.

1.5 Conclusion

This thesis has presented the design, construction, and initial operation of a precision spectroscopy apparatus for studying atomic transitions in neutral Ytterbium at 398.911 nm, using a tunable external cavity diode laser (ECDL). The work was carried out over a period of approximately three months. The Doppler-broadened absorption spectrum of the ${}^1S_0 \rightarrow {}^1P_1$ transition of Ytterbium was successfully recorded, confirming correct laser wavelength targeting and efficient atomic beam production from the effusive oven source. The observed Gaussian lineshape and the presence of isotope-resolved features within the Doppler envelope are in qualitative agreement with theoretical predictions based on the Maxwell–Boltzmann velocity distribution.

Saturation absorption spectroscopy was subsequently implemented using counter-

propagating pump and probe beams. While a hint of a sub-Doppler feature was observed near the expected transition wavelength in certain pump power settings, a fully resolved and reproducible Lamb dip was not obtained within the measurement conditions of this project. The result is attributed to insufficient signal-to-noise ratio in the differential detection scheme, sensitivity to optical alignment, and most possible contributions from stray reflections from the vacuum chamber windows. These are recognised experimental challenges that require systematic optimisation before the technique can be used for quantitative frequency measurements.

The complete optical apparatus for cross-beam saturated absorption spectroscopy (CBSAS) was assembled and aligned. The theoretical basis of CBSAS, including the inherent frequency shift arising from the orthogonal beam geometry and the requirement for a calibrated SAS reference, was analysed and discussed. It was established that SAS optimisation is a necessary prerequisite before CBSAS measurements can be meaningfully performed and interpreted.

The Fabry–Perot interferometer was integrated as wavelength-meter into the setup for frequency calibration of the laser sweep using the free spectral range as a frequency ruler, which will be essential for absolute frequency measurements in future work.

Overall, this project has successfully established the experimental infrastructure for high-resolution Doppler-free spectroscopy of Ytterbium. The theoretical framework, experimental apparatus, and diagnostic tools are in place for future precision measurements of hyperfine splittings and isotope shifts, which have direct relevance to atomic clock development, laser cooling, and fundamental symmetry tests.

1.6 Future Outlook

The present work lays the groundwork for a comprehensive programme of precision spectroscopy measurements on Ytterbium. Several well-defined steps are identified for future work.

1.6.1 Optimisation of the SAS Signal

The immediate priority is to obtain a clean, reproducible Lamb dip in the conventional counter-propagating SAS configuration. This requires a systematic approach to noise reduction and alignment optimisation. Specifically, the signal-to-noise ratio of the differential detection scheme should be improved by implementing balanced photodetection, in which the two probe beam signals are subtracted using a balanced detector rather than post-processing. This technique significantly suppresses common-mode laser intensity noise, which is the dominant noise source in the current setup.

The optical alignment of the counter-propagating beams should be verified inter-

ferometrically to ensure strict collinearity, as even small angular deviations broaden or eliminate the Lamb dip. The contribution of stray reflections from the vacuum chamber windows should also be investigated, for example by measuring the spectrum with the pump beam blocked at different positions in the beam path to isolate the source of spurious signals. Anti-reflection coated vacuum viewports would eliminate this problem entirely and should be considered for the next generation of the apparatus.

1.6.2 Cross-Beam Saturated Absorption Spectroscopy

Once a clean SAS signal has been established as a frequency reference, the CBSAS apparatus, which is already constructed and aligned, can be commissioned for operation. The first measurements should focus on verifying the expected frequency shift between the SAS and CBSAS resonances as a function of the intersection angle between the pump and probe beams. Comparison of the linewidths obtained in the two configurations will allow a direct quantitative assessment of the reduction in power broadening offered by the orthogonal geometry, which is the principal motivation for CBSAS.

1.6.3 Hyperfine Structure and Isotope Shift Measurements

With Doppler-free resolution established, the apparatus can be used to resolve the hyperfine structure of the odd isotopes of Ytterbium (^{171}Yb and ^{173}Yb), which possess nuclear spin $I = 1/2$ and $I = 5/2$ respectively, giving rise to hyperfine splittings of the excited $^1P_1$ state. Accurate determination of these splittings, using the Fabry–Perot interferometer for frequency calibration, will provide a benchmark for comparison with theoretical calculations of nuclear structure.

1.6.4 Laser Frequency Stabilisation

The narrow Doppler-free resonances obtained from SAS or CBSAS can serve as frequency references for locking the laser frequency using standard locking techniques. A frequency-stabilised laser at 398.911 nm is an essential tool for Zeeman slowing and magneto-optical trapping of Ytterbium atoms. Achieving laser cooling and trapping of Ytterbium will open the way for further precision measurements in an ultracold environment, with dramatically reduced Doppler and collisional broadening.

1.6.5 Ion Trap Integration

In the longer term, the precision spectroscopy techniques developed in this work can be extended to trapped Ytterbium ions. Ion trapping eliminates motional broadening

entirely through the Lamb–Dicke confinement regime, enabling spectroscopy at or near the natural linewidth. This would provide the highest possible frequency resolution for measurements relevant to optical atomic clock development and tests of fundamental physics, including searches for time variation of fundamental constants in my laboratory.

Chapter 2

Precision Spectroscopy

2.1 Introduction

Ion traps are the leading platforms tools for experimental explanations of Atomic, Molecular and Optical physics. Traps has important role in mostly precision spectroscopy, atomic clocks and mass spectrometry, where quadrupole radio-frequency fields are used to as a advantage for the stability properties of the equations of motion of ions.

Ion traps allowed to a charged particle float in empty space, without touching any container for a very long time. Such confinement helps to observe the isolated particles (even a single ion) and allows measurements of their properties with highly precision. Paul said that trapping charged particles without touching any physical walls helps to scientists study a single atom or ion directly, instead of measuring many particles together (which is only an average result). This highly improves precision measurements.

The idea of such traps did not appear suddenly , it came from earlier techniques used in molecular beams, mass spectrometers, and particle accelerators. In recent years,Ion traps is not only simply confine ions; for quantum information processing and for high-precision experiments applications (such as testing fundamental physical symmetries and searching for the electron's electric dipole moment), ions must be transported, separated and recombined in a controlled way. These applications often use surface ion traps with ring-like (toroidal) trapping regions, where ions follow fixed paths along closed loops.

2.2 Theory

2.2.1 Electrostatic Constraints and Dynamic Stabilization

For an ion to be trapped at a fixed position in space, it must be confined in all three spatial dimensions by a restoring force that increases linearly with displacement from the equilibrium point. Such confinement corresponds to motion in a parabolic potential. However, in regions free of charge, the electrostatic potential must satisfy Laplace's equation,

$$\nabla^2 V = \frac{\partial^2 V}{\partial x^2} + \frac{\partial^2 V}{\partial y^2} + \frac{\partial^2 V}{\partial z^2} = 0. \tag{2.1}$$

To understand why static trapping is impossible, consider a quadratic potential of the form

$$V(x, y, z) = \alpha x^2 + \beta y^2 + \gamma z^2, \tag{2.2}$$

which would provide simultaneous confinement in all three directions if α, β, and γ were all positive. Substituting this into Laplace's equation immediately gives the constraint

$$\alpha + \beta + \gamma = 0. \tag{2.3}$$

Since the three coefficients must sum to zero, at least one of them must be negative, meaning the potential is repulsive in at least one direction. This result is the mathematical expression of Earnshaw's theorem: a charged particle cannot be held in stable static equilibrium by electrostatic forces alone. This fundamental limitation motivated the development of dynamically stabilized traps that use time-dependent electric fields instead.

2.2.2 Radio-Frequency Quadrupole Fields

Dynamic stabilization is achieved by applying a time-dependent electric field whose sign alternates periodically. In a quadrupole configuration, the potential is quadratic in Cartesian coordinates and satisfies Laplace's equation. A two-dimensional quadrupole field is obtained by setting $\alpha = -\beta$ and $\gamma = 0$, giving

$$V(x, y) = \alpha(x^2 - y^2). \tag{2.4}$$

Under a static applied voltage, an ion is focused in one transverse direction but defocused in the other, so confinement is not possible. When the voltage alternates periodically, however, the focusing and defocusing directions swap in time. Because

the electric field is inhomogeneous, the time-averaged force does not cancel exactly: a small net restoring force remains, always directed toward regions of weaker field. Under suitable conditions this produces stable, bounded motion.

When the applied voltage takes the form $U - V\cos\Omega t$, where U is a static (DC) component and V is the amplitude of the radio-frequency (RF) component at drive frequency Ω, the equations of motion in the x and y directions reduce to the Mathieu differential equation,

$$\frac{d^2u}{d\tau^2} + (a_u - 2q_u\cos 2\tau)\,u = 0, \tag{2.5}$$

where $\tau = \Omega t/2$ and the dimensionless stability parameters are

$$a_u = \frac{4eU}{mr_0^2\Omega^2}, \qquad q_u = \frac{2eV}{mr_0^2\Omega^2}, \tag{2.6}$$

with e the ion charge, m the ion mass, and r_0 the distance from the trap axis to the nearest electrode. A key feature of the Mathieu equation is that the stability of the solution depends only on a and q and not on the initial position or velocity of the ion. In the a–q parameter space there exist well-defined regions of stable (bounded) and unstable (unbounded) motion, as shown in Figure 2.1. When only an RF voltage is applied ($U = 0$, so $a = 0$), the relevant parameter is q alone, and stable confinement requires $q \lesssim 0.908$.

2.2.3 Ion Motion: Secular Motion and Micromotion

For stability parameters satisfying $q \ll 1$, an approximate analytical solution to the Mathieu equation can be written as

$$u(t) \approx u_0\left[1 + \frac{q}{2}\cos(\Omega t)\right]\cos(\omega_{\text{sec}}\,t + \phi), \tag{2.7}$$

where u_0 is the amplitude, ϕ is an arbitrary phase, and ω_{sec} is the secular frequency given by

$$\omega_{\text{sec}} \approx \frac{\Omega}{2}\sqrt{a + \frac{q^2}{2}}. \tag{2.8}$$

This solution reveals two distinct types of motion superimposed on each other. The first is a slow harmonic oscillation at frequency $\omega_{\text{sec}} \ll \Omega$, called *secular motion*, which describes the smooth drift of the ion within the trap. The second is a rapid oscillation at the drive frequency Ω, called *micromotion*, whose amplitude is modulated by the secular displacement u_0. Because the micromotion amplitude scales with distance from the trap center, an ion displaced from the axis by any stray DC field will exhibit enhanced micromotion beyond the unavoidable intrinsic level; this excess is called

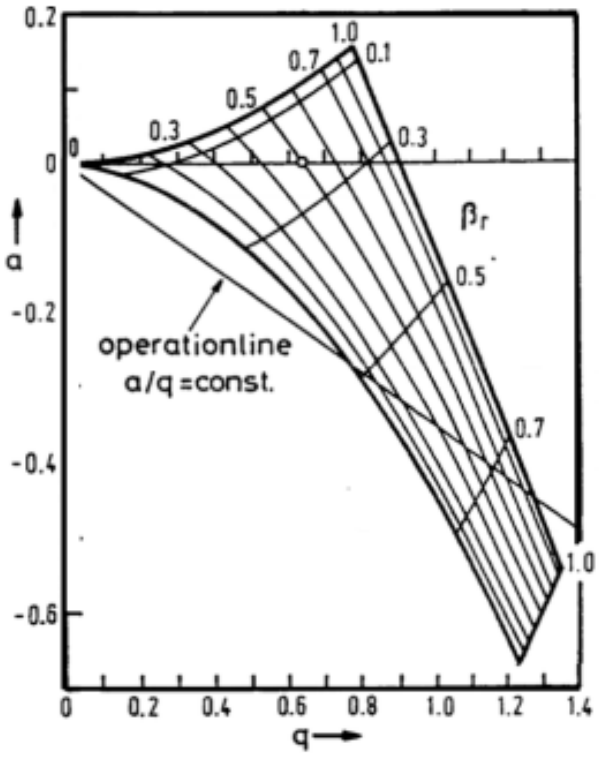

Figure 2.1: Lowest stability region in the a–q parameter space of the Mathieu equation. Bounded ion trajectories exist only within the shaded region. The simulation parameters used in this work ($a = 0.01$, $q = 0.2$ and $a = 0.1$, $q = 0.65$) both lie inside the stable zone.

excessive micromotion.

2.2.4 The Pseudopotential Approximation

A physically transparent way to understand secular confinement is through the pseudopotential approximation. In an inhomogeneous time-varying field, the time-averaged effect of the rapid micromotion produces an effective static potential. For an ion with charge e and mass m in an RF field of amplitude V and frequency Ω, the pseudopotential is

$$\Psi = \frac{e^2 V^2}{4m\Omega^2} \left|\nabla\phi(x, y, z)\right|^2, \tag{2.9}$$

where ϕ is the spatial part of the electric potential normalised to unit voltage. Crucially, substituting the quadrupole potential $\phi \propto x^2 - y^2$ into the gradient squared yields a result proportional to $x^2 + y^2$: a bowl-shaped potential that provides genuine confinement at the trap axis. The secular frequency can then be recovered directly from the curvature of Ψ.

2.3 Simulation of Three-Dimensional Ion Traps

A true ion trap requires confinement in all three spatial dimensions. This can be achieved by choosing the potential coefficients as $\alpha = \beta = 1$ and $\gamma = -2$, which generates a three-dimensional quadrupole field. In cylindrical coordinates, this configuration has the same functional form as the two-dimensional case, with the axial direction scaled by a factor of two. The equations of motion are again of Mathieu form, with the stability parameters modified by this geometric factor.

2.3.1 Geometry of the Trap

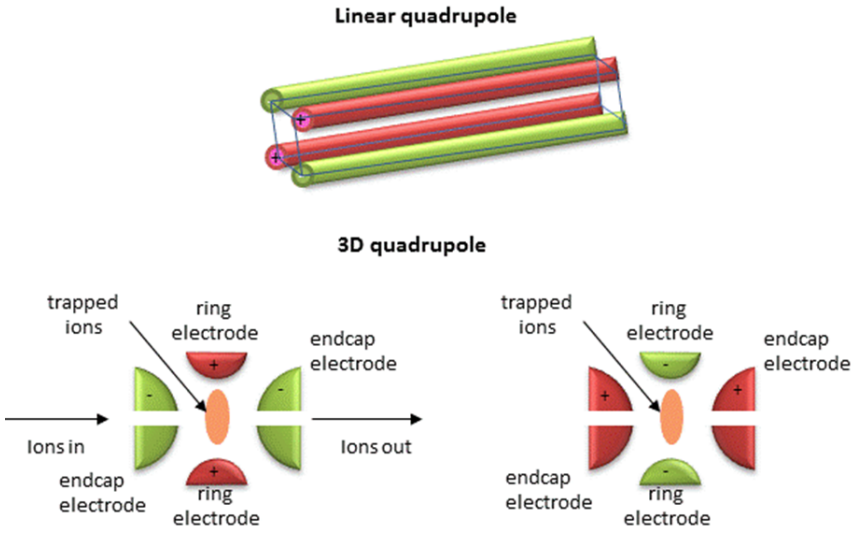

Figure 2.2: Schematic diagram of a quadrupole ion trap. (Image: Unknown Author, CC BY-NC.)

The theoretical framework above assumes an ideal quadrupole potential, but a practical question remains: how can such a potential be physically generated? The answer rests on a uniqueness principle from electrostatics — if the potential is specified on a closed boundary, it is uniquely determined everywhere inside. Therefore, electrodes shaped to coincide with equipotential surfaces of the desired potential will, when biased to the corresponding voltages, reproduce that potential in the interior region.

Hyperbolic electrode geometries realise this idea exactly and are therefore the theoretical ideal. In practice, however, they present serious difficulties:

- precision machining of hyperbolic surfaces is technically demanding and expensive;

- the bulky three-dimensional structure restricts optical access, making laser addressing and ion imaging difficult;
- the trap performance is sensitive to small alignment errors.

These difficulties motivate the use of simpler, more easily fabricated geometries that approximate the ideal quadrupole potential sufficiently well in the trapping region, even if higher-order multipole components are introduced elsewhere.

A widely used practical design is the *four-rod* (or linear Paul) trap, in which the hyperbolic electrodes are replaced by four parallel cylindrical rods arranged symmetrically around the trap axis. Applying RF voltages to diagonally opposite pairs of rods generates an electric field that closely approximates the ideal quadrupole potential in the transverse plane, providing effective radial confinement. However, the potential is uniform along the axial direction, so ions are not confined along the trap axis by the RF field alone.

Full three-dimensional confinement is achieved by adding a pair of *endcap* electrodes at the two ends of the rod assembly, biased with a static (DC) voltage. The combined fields then confine the ion in all three dimensions:

- the RF quadrupole field provides dynamic radial confinement;
- the DC endcap field provides static axial confinement.

This configuration supports the trapping of single ions as well as extended linear ion chains, which are important for quantum information processing with trapped ions.

2.3.2 Ion Motion in the Trap

To study the confinement dynamics, we numerically integrated the Mathieu equations of motion using the fourth-order Runge–Kutta method implemented in Python. Trajectories were computed for two representative parameter sets, $(a, q) = (0.01, 0.20)$ and $(a, q) = (0.1, 0.65)$, both lying within the first stability region. The simulated time span of 10^5 RF cycles is long enough to confirm that the trajectories remain bounded, demonstrating stable trapping.

The simulated trajectories clearly exhibit the two-component structure predicted analytically. Slow oscillations at the secular frequency ω_{sec} are modulated by rapid micromotion at the drive frequency Ω. As expected from the pseudopotential picture, the micromotion amplitude grows with displacement from the trap center: an ion displaced by a stray DC field shows *excessive micromotion* whose amplitude increases with radial distance. In a real trap this effect arises from electrode misalignment

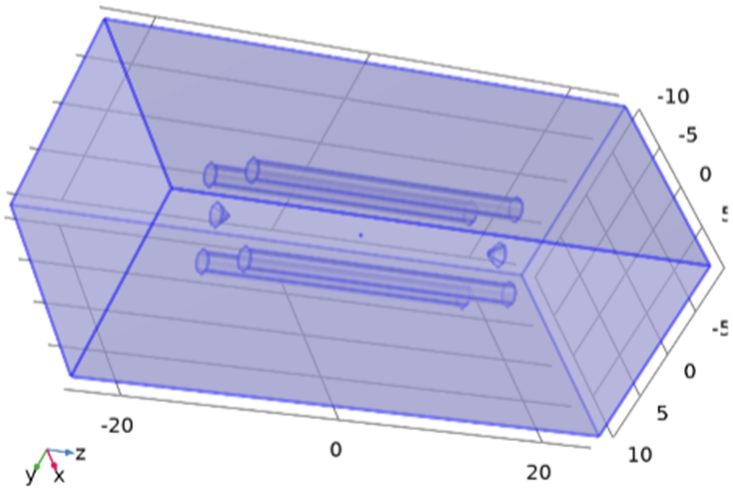

Figure 2.3: Simulated geometry of the four-rod quadrupole ion trap used in the numerical study.

or stray charges and must be minimised by applying compensating DC voltages to dedicated electrodes.

Replacing the ideal hyperbolic geometry with cylindrical rods introduces higher-order multipole components in the electric field, as confirmed by COMSOL electrostatic simulations. While these imperfections do not destroy stability within the first Mathieu region, they do impose an upper limit on the ion temperature that can be tolerated before the ion escapes the trap.

2.4 Results and Discussion

The performance of an ion trap is governed by the ability to generate a stable potential well capable of confining charged particles against kinetic heating and background noise. In this section, we present numerical simulation results obtained via the fourth-order Runge–Kutta (RK4) method to analyze the stability and dynamics of ions within a quadrupolar field. To provide independent validation, the same Mathieu equations were also solved using Mathematica's built-in integrator and the Finite Difference Method (FDM), allowing a direct three-way comparison of numerical approaches.

2.4.1 Validation of Trapping Conditions

To confirm stable confinement, we numerically integrated the Mathieu equations of motion for two representative parameter sets chosen to lie within the first stability region of the a–q diagram:

- Case 1: $(a = 0.01,\ q = 0.20)$ — deep inside the stability region, representing a near-ideal low-q operating point.
- Case 2: $(a = 0.10,\ q = 0.65)$ — closer to the stability boundary, where secular oscillation amplitudes are noticeably larger.

Each trajectory was evolved over 10^5 RF cycles, a duration long enough to confirm that the motion remains bounded and does not diverge. Figures 2.4–2.6 show the results for Case 1, while Figures 2.7–2.9 show the results for Case 2.

Case 1: $a = 0.01,\ q = 0.20$

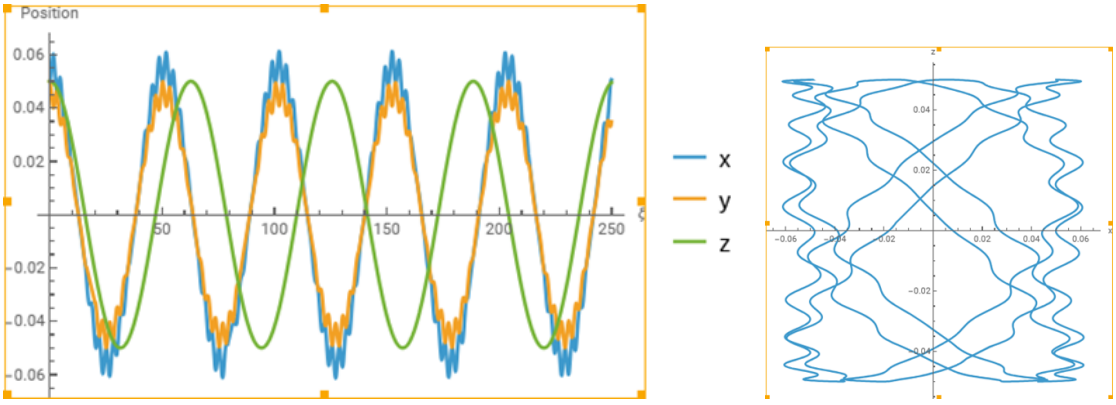

Figure 2.4: Ion trajectory for $a = 0.01$, $q = 0.20$ solved via Mathematica. The left panel shows position versus time; the right panel shows the corresponding phase-space projection. Both secular motion and superimposed micromotion are clearly visible.

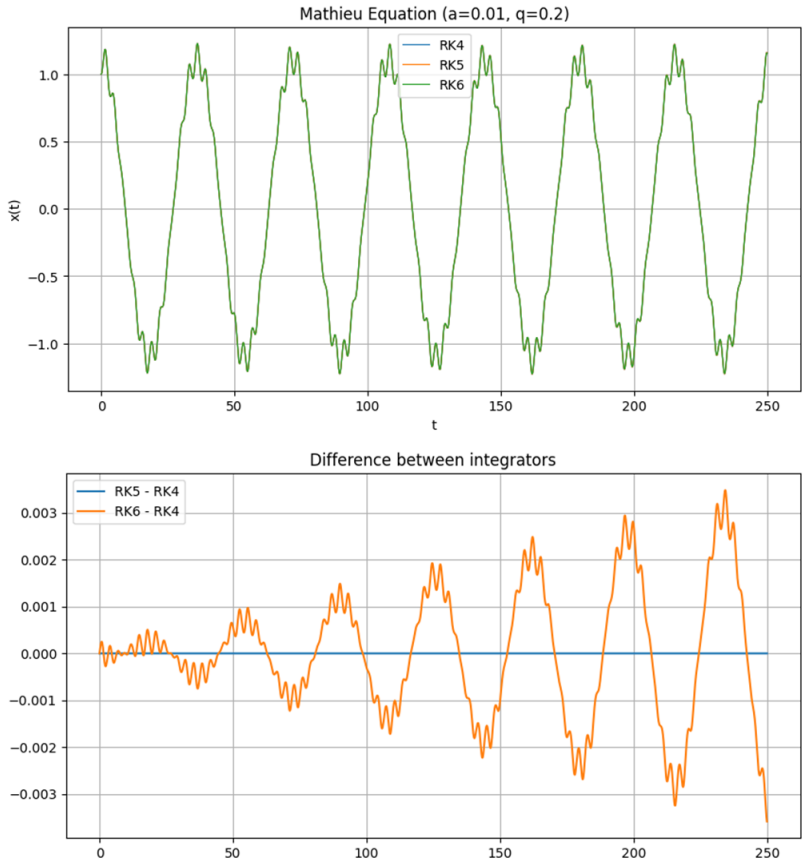

Figure 2.5: Ion trajectory for $a = 0.01$, $q = 0.20$ obtained via the fourth-order Runge–Kutta method. The upper panel compares RK4, RK5, and RK6 integrators; the lower panel shows the difference between them, confirming numerical convergence to within $\sim 10^{-3}$ over the full simulation window.

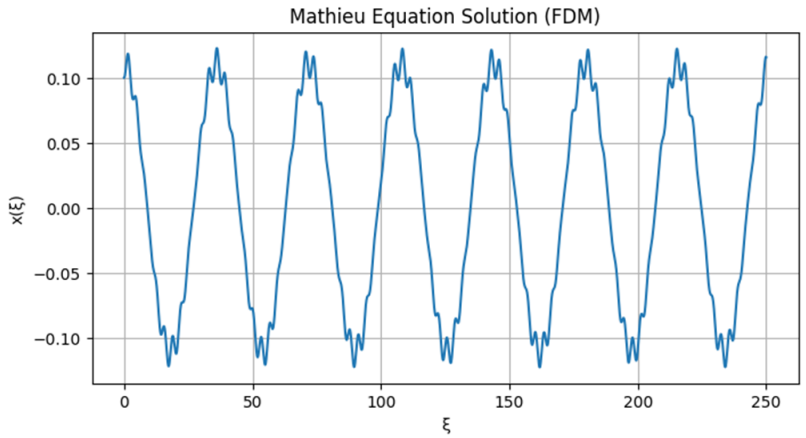

Figure 2.6: Ion trajectory for $a = 0.01$, $q = 0.20$ obtained via the Finite Difference Method. The bounded, oscillatory character is consistent with the RK and Mathematica results, confirming method-independent stability.

For Case 1, all three methods agree closely. The ion maintains a stable, bounded trajectory throughout the 10^5-cycle simulation. The trajectory exhibits the characteristic two-component structure predicted by the analytical solution: slow secular oscillations at frequency $\omega_{\text{sec}} \ll \Omega$ envelope rapid micromotion at the drive frequency Ω. At the low q value of 0.20, the micromotion amplitude is small relative to the secular amplitude, consistent with the $q/2$ prefactor in the analytical approximation.

The small but nonzero differences between the RK4, RK5, and RK6 integrators visible in Figure 2.5 grow slowly over time, as expected for any explicit integrator applied to a non-autonomous oscillator. The magnitude of these differences remains below 10^{-3} over the full simulation window, demonstrating that RK4 is sufficiently accurate for the present study.

Case 2: $a = 0.10,\ q = 0.65$

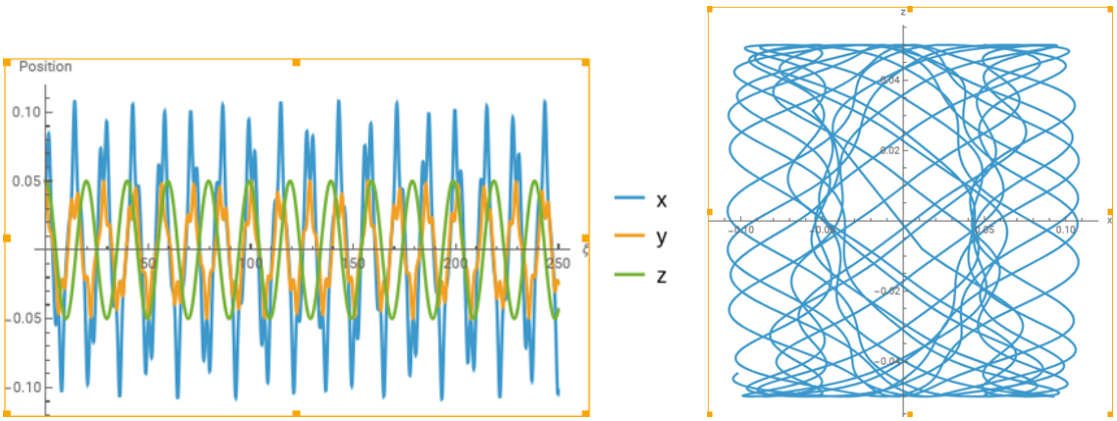

Figure 2.7: Ion trajectory for $a = 0.10$, $q = 0.65$ solved via Mathematica. The increased q value produces visibly larger secular oscillation amplitudes and more pronounced micromotion compared to Case 1. The phase-space projection (right) shows a more complex Lissajous-like pattern reflecting the stronger coupling between the two transverse degrees of freedom.

For Case 2, the trajectory remains stable but displays noticeably larger oscillation amplitudes in both the secular and micromotion components. This is consistent with the larger q value placing the operating point closer to the stability boundary, where the ion explores a greater volume of the trap. The inter-method agreement remains good, though the RK integrator differences are slightly larger than in Case 1, as expected when the trajectory amplitude is greater.

2.4.2 Two-Component Motion: Secular and Micromotion

Both simulation cases confirm the two-component structure of ion motion that was derived analytically in the Theory section. The secular motion is a slow, smooth oscillation whose frequency ω_{sec} is set by the trap parameters through

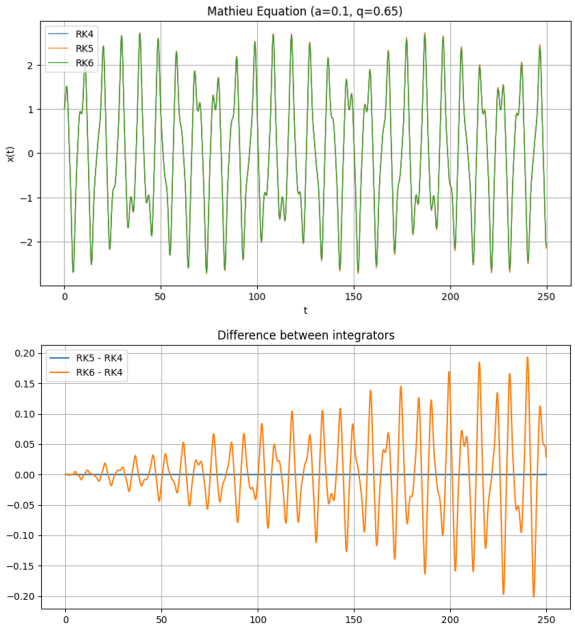

Figure 2.8: Ion trajectory for $a = 0.10$, $q = 0.65$ via the Runge–Kutta method. The left panel shows the time-domain trajectory; the right panel shows integrator differences, which are larger than in Case 1 but remain bounded, confirming numerical stability.

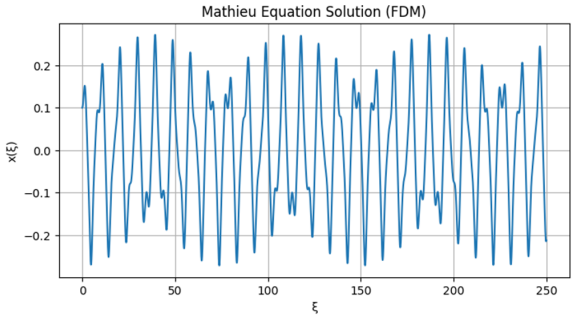

Figure 2.9: Ion trajectory for $a = 0.10$, $q = 0.65$ via the Finite Difference Method, consistent with the other two solvers.

$$\omega_{\text{sec}} \approx \frac{\Omega}{2}\sqrt{a + \frac{q^2}{2}}. \tag{2.10}$$

Superimposed on this is the micromotion, a rapid oscillation at the drive frequency Ω whose amplitude at any instant is proportional to the instantaneous secular displacement. As a result, the micromotion is smallest when the ion passes through the trap center and largest at the turning points of the secular oscillation.

A key observation from the simulations is that this amplitude modulation of the micromotion is more pronounced in Case 2 ($q = 0.65$) than in Case 1 ($q = 0.20$). This is again consistent with the analytical solution, in which the micromotion prefactor scales as $q/2$: larger q means stronger micromotion at any given secular displacement.

2.4.3 Effect of Electrode Geometry: Multipole Imperfections

The simulations above assume an ideal quadrupole field. In practice, the four-rod trap geometry introduces deviations from the perfect quadrupole because cylindrical rods only approximate hyperbolic surfaces. To assess the magnitude of these imperfections, COMSOL Multiphysics electrostatic simulations were performed for the four-rod geometry shown in Figure 2.3.

The simulated potential was decomposed into multipole components. The dominant contribution is the desired quadrupole term, but higher-order multipoles (principally octupole and dodecapole components) are also present. Within the first Mathieu stability region, these higher-order terms do not destroy confinement: the ion trajectory remains bounded because the quadrupole term dominates near the trap axis. However, the anharmonic components of the potential set a practical upper limit on the ion temperature. An ion with sufficient kinetic energy samples regions farther from the axis where the higher-order terms become significant, leading to amplitude-dependent shifts in the secular frequency and, ultimately, to parametric heating and ion loss.

This result has a direct implication for the Yb^+ trap targeted in this work: laser cooling must reduce the ion temperature sufficiently that the ion remains in the near-axis region where the quadrupole approximation holds. The electrode dimensions and rod-to-axis distance should also be optimised in future designs to minimise the ratio of octupole to quadrupole amplitude.

2.4.4 Excessive Micromotion and its Sources

Beyond the intrinsic micromotion that is always present in a Paul trap, real traps suffer from *excessive micromotion* arising from two main sources. First, stray static electric fields — from patch charges on electrode surfaces, contact potentials, or imperfect

voltage sources — displace the ion from the RF null at the trap axis. At any displaced position, the ion experiences a non-zero RF field even at the secular turning points, which drives additional micromotion. Second, electrode misalignment shifts the RF null away from the geometric center, so that even a perfectly compensated ion sits off-axis.

In the present simulations the trap geometry was taken to be ideal, so excessive micromotion was not modelled explicitly. Confirming this analytically: at the trap center the RF electric field vanishes by symmetry, so the pseudopotential gradient is zero and no excess micromotion is driven. Any future experimental realisation will require active micromotion compensation using additional DC electrodes to null the stray fields.

2.5 Conclusion

This work has presented a theoretical and numerical study of ion confinement in a Paul trap, motivated by the goal of designing a linear trap for Yb^+ ions suited to precision spectroscopy and quantum technology applications.

On the theoretical side, we showed from first principles why static electric fields cannot confine a charged particle (Earnshaw's theorem) and how this limitation is overcome by time-varying RF quadrupole fields. The equations of motion reduce to the Mathieu differential equation, whose solutions are characterised entirely by the dimensionless parameters a and q. Stable, bounded trajectories exist only within specific regions of the a–q plane, and the ion motion within these regions naturally decomposes into slow secular oscillations and fast micromotion.

On the numerical side, Mathieu trajectories were computed using three independent methods — Mathematica, the fourth-order Runge–Kutta method, and the Finite Difference Method — for two parameter sets representative of the first stability region. All three methods produced consistent results, with inter-method differences remaining below 10^{-3} over 10^5 RF cycles for the lower-q case. This cross-validation establishes confidence in the computational framework and confirms that RK4 is an efficient and sufficiently accurate integrator for trajectory-level trap simulations.

The simulations directly verified the two-component structure of ion motion: secular oscillations at $\omega_{\text{sec}} \ll \Omega$ modulated by micromotion at Ω, with the micromotion amplitude scaling with secular displacement as predicted analytically. The pseudopotential picture was shown to be consistent with the full numerical results, providing a reliable time-averaged description of confinement.

COMSOL electrostatic simulations of the four-rod geometry confirmed that replacing ideal hyperbolic electrodes with cylindrical rods introduces higher-order multipole components. These do not destroy stability but limit the maximum ion temperature

and motivate careful optimisation of electrode dimensions in the experimental design.

Taken together, these results establish a solid theoretical and computational foundation for the next stage of the project: the physical construction and characterisation of a linear Paul trap for Yb^+.

2.6 Future Outlook

The present study focused on single-ion dynamics in an idealised trap geometry. Several important directions remain open for future work, both on the simulation side and toward the experimental realisation of the Yb^+ trap.

2.6.1 Micromotion Compensation and Segmented Electrodes

The most immediate experimental requirement is robust micromotion compensation. Future trap designs should incorporate segmented DC electrodes along the axial direction. Segmentation serves two purposes: it allows independent control of the axial potential to create well-defined ion-chain configurations, and it provides additional degrees of freedom to null stray DC fields that would otherwise displace the ion from the RF null and drive excessive micromotion. Achieving near-zero micromotion at the trap center is essential for high-coherence operations and for reaching the Lamb–Dicke regime required for resolved-sideband laser cooling of Yb^+.

2.6.2 Electrode Geometry Optimisation

The COMSOL simulations showed that the four-rod geometry introduces higher-order multipole components whose relative magnitude depends on the ratio of the rod radius to the rod-to-axis distance. A systematic parameter sweep in COMSOL over this geometric ratio, combined with a multipole decomposition of the resulting field, would identify the electrode dimensions that minimise anharmonic contributions while remaining practically fabricable. Blade-type or tapered rod geometries could also be explored as alternatives that more closely approximate the hyperbolic profile.

2.6.3 Multi-Ion Simulations and Coulomb Crystals

The current simulation framework handles a single ion. Extending the code to include the Coulomb repulsion between multiple ions would allow the study of linear ion chains and planar Coulomb crystals. Such structures are directly relevant to quantum information processing with Yb^+, where entangling gates rely on the collective motional modes of the chain. Simulating the normal-mode spectrum as a function

of trap parameters and ion number would guide the choice of operating point for multi-qubit experiments.

2.6.4 Laser Cooling Dynamics

A natural next step in the simulation programme is to include a simplified laser-cooling model — for example, a velocity-dependent damping force representing Doppler cooling on the ${}^2S_{1/2} \rightarrow {}^2P_{1/2}$ transition of Yb^+ at 369.5 nm. Coupling the cooling dynamics to the trap simulation would allow prediction of the steady-state ion temperature, comparison with the Doppler cooling limit, and assessment of how quickly the ion thermalises after loading. This would directly inform the experimental loading and cooling sequence.

2.6.5 Integration with Spectroscopy Goals

The longer-term objective of this project is precision spectroscopy of Yb^+ transitions relevant to atomic clock and quantum technology applications. The trap design parameters established in this work — secular frequency, trap depth, micromotion level — feed directly into the spectroscopic performance. In particular, the second-order Doppler shift from residual secular motion and the micromotion-induced sideband structure both depend on the trap operating point. Future simulations should therefore evaluate these systematic frequency shifts quantitatively, connecting the trap physics directly to the spectroscopic accuracy budget.

2.6.6 Experimental Realisation

On the experimental side, the immediate next steps are the mechanical design and fabrication of the four-rod trap, followed by the assembly of the vacuum system, ion source, and laser cooling optics. The numerical results presented here provide a starting point for the choice of trap dimensions and RF drive parameters. Once the trap is operational, the simulation framework developed in this work can be used to cross-check experimentally measured secular frequencies and micromotion levels against the theoretical predictions, closing the loop between simulation and experiment.

Bibliography

[1] S. Utreja, P. Roy, H. Rathore, S. Choudhury, M. Das, and S. Panja, Optics Communications **285**, 4685 (2012).

[2] D. W. Preston, American Journal of Physics **64**, 1432 (1996).

[3] Massachusetts Institute of Technology, Doppler-free spectroscopy experiment, `https://web.mit.edu/8.13/www/JLExperiments/JLExp48.pdf` (2026), online.

[4] V. S. Letokhov, *Nonlinear Laser Spectroscopy* (Springer, 1977).

[5] K. B. MacAdam, A. Steinbach, and C. Wieman, American Journal of Physics **60**, 1098 (1992).

[6] Max Planck Institute of Quantum Optics, Saturation spectroscopy, `https://www.mpq.mpg.de/4992695/saturation_spectroscopy.pdf` (2026), online.

[7] Reed College Physics Department, Doppler-free saturated absorption spectroscopy, `https://www.reed.edu/physics/332/pdf/Doppler_Free.pdf` (2026), online.

[8] J. Vanier and C. Audoin, Optics Letters **41**, 2982 (2016).

[9] A. Author and B. Author, arXiv preprint arXiv:2404.14734 (2024).

[10] M. D. Swallows *et al.*, arXiv preprint arXiv:1109.0434 (2011).

[11] W. Paul, Electromagnetic traps for charged and neutral particles (1989), nobel Lecture, December 8.

[12] N. Batra, *Computations, design and instrumentation for precision ion trap experiment*, Ph.D. thesis, AcSIR, CSIR-National Physical Laboratory (2018).

[13] T. Taylor, *Simulation and design of ion traps using the method of fundamental solutions*, Master's thesis, University of Nevada, Las Vegas (2024).

[14] COMSOL Multiphysics, Radio frequency quadrupole ion trap model (2024), application Gallery.

[15] R. E. March and J. F. J. Todd, *Quadrupole Ion Trap Mass Spectrometry* (Wiley, 1995).

[16] A. N. Krutchinsky *et al.*, Journal of the American Society for Mass Spectrometry (1998).

[17] J. Roijer, *Tools for applied soft ionization mass spectrometry*, Ph.D. thesis, Uppsala University (2012).

[18] R. N. Zare *et al.*, Analytical Chemistry (2014).

[19] B. A. S. A., *Development of a laminar construction quadrupole ion trap*, Master's thesis, University of New Orleans (2006).

[20] Purdue University, *Development of an electrostatic linear ion trap as a standalone tandem mass spectrometer*, Ph.D. thesis (2007).

[21] ETH Zurich TIQI Group, Trapped ion quantum information group master's theses archive (2026), web archive.

[22] Naval Postgraduate School, *Ion trap quantum computing*, Master's thesis (2012).

[23] S. Researcher, *An integrated fiber-based cavity in a Paul trap*, Master's thesis, Johannes Gutenberg University Mainz (2021).

[24] A. Name, Nature Communications (2026).

Appendix A

Appendix

An atom possesses a natural transition frequency ω_0 in its rest frame. However, when the atom moves with velocity $\mathbf{v}$ relative to the laboratory frame, the frequency of the incident radiation is Doppler shifted. The observed angular frequency in the laboratory frame is given by

$$\omega' = \omega - \mathbf{k} \cdot \mathbf{v}, \tag{A.1}$$

where $\mathbf{k}$ is the wavevector of the radiation. Only the component of velocity along the propagation direction contributes to the Doppler shift.

For simplicity, we assume both $\mathbf{k}$ and $\mathbf{v}$ are along the z-axis, so that

$$\mathbf{k} \cdot \mathbf{v} = kv. \tag{A.2}$$

The magnitude of the wavevector is

$$k = \frac{\omega}{c} = \frac{2\pi}{\lambda}, \tag{A.3}$$

where c is the speed of light and λ is the wavelength.

Resonant absorption occurs when the radiation is resonant in the atom's rest frame, i.e., $\omega' = \omega_0$. The detuning is defined as

$$\delta \equiv \omega' - \omega_0 = kv. \tag{A.4}$$

Substituting $k = \omega_0/c$, we obtain

$$\delta = \frac{\omega_0 v}{c}. \tag{A.5}$$

This shows that atoms with different velocities interact with different frequencies, leading to Doppler broadening.

In thermal equilibrium, atomic velocities follow the Maxwell–Boltzmann distribu-

tion. The probability of finding atoms with velocities between v and $v + dv$ is

$$f(v)\,dv = \sqrt{\frac{M}{2\pi k_B T}} \exp\left(-\frac{Mv^2}{2k_B T}\right) dv, \tag{A.6}$$

where M is the atomic mass, k_B is Boltzmann's constant, and T is the temperature.

Defining the most probable speed

$$u = \sqrt{\frac{2k_B T}{M}}, \tag{A.7}$$

the distribution can be rewritten as

$$f(v)\,dv = \frac{1}{u\sqrt{\pi}} \exp\left(-\frac{v^2}{u^2}\right) dv. \tag{A.8}$$

Using the Doppler relation

$$\delta = kv = \frac{\omega_0}{c} v, \tag{A.9}$$

we express the velocity in terms of frequency as

$$v = \frac{c}{\omega_0}(\omega - \omega_0). \tag{A.10}$$

To obtain the spectral line shape, we transform the velocity distribution into a frequency distribution:

$$g(\omega)\,d\omega = f(v)\,dv. \tag{A.11}$$

Since

$$dv = \frac{c}{\omega_0} d\omega, \tag{A.12}$$

the Doppler-broadened line shape becomes

$$g_D(\omega) = \frac{c}{u\omega_0\sqrt{\pi}} \exp\left[-\frac{c^2}{u^2}\left(\frac{\omega - \omega_0}{\omega_0}\right)^2\right]. \tag{A.13}$$

This is a Gaussian profile centered at $\omega = \omega_0$, satisfying

$$\int_{-\infty}^{\infty} g_D(\omega)\,d\omega = 1. \tag{A.14}$$

The maximum value occurs at $\omega = \omega_0$:

$$g_D(\omega_0) = \frac{c}{u\omega_0\sqrt{\pi}}. \tag{A.15}$$

To find the full width at half maximum (FWHM), we impose the condition

$$g_D(\omega_0 + \delta_{1/2}) = \frac{1}{2} g_D(\omega_0), \tag{A.16}$$

where $\delta_{1/2}$ is the half-width at half maximum.

Substituting into the Gaussian expression:

$$\frac{c}{u\omega_0\sqrt{\pi}} \exp\left[-\frac{c^2}{u^2}\left(\frac{\delta_{1/2}}{\omega_0}\right)^2\right] = \frac{1}{2} \cdot \frac{c}{u\omega_0\sqrt{\pi}}. \tag{A.17}$$

Canceling the common prefactor, we obtain

$$\exp\left[-\frac{c^2}{u^2}\left(\frac{\delta_{1/2}}{\omega_0}\right)^2\right] = \frac{1}{2}. \tag{A.18}$$

Taking the natural logarithm on both sides:

$$-\frac{c^2}{u^2}\left(\frac{\delta_{1/2}}{\omega_0}\right)^2 = \ln\left(\frac{1}{2}\right). \tag{A.19}$$

Using $\ln(1/2) = -\ln 2$, this simplifies to

$$\frac{c^2}{u^2}\left(\frac{\delta_{1/2}}{\omega_0}\right)^2 = \ln 2. \tag{A.20}$$

Solving for $\delta_{1/2}$:

$$\delta_{1/2} = \frac{u\omega_0}{c}\sqrt{\ln 2}. \tag{A.21}$$

The full width at half maximum is defined as

$$\Delta\omega_D = 2\delta_{1/2}, \tag{A.22}$$

therefore,

$$\Delta\omega_D = 2\frac{u\omega_0}{c}\sqrt{\ln 2}. \tag{A.23}$$

Dividing by ω_0, we obtain

$$\frac{\Delta\omega_D}{\omega_0} = 2\sqrt{\ln 2}\,\frac{u}{c}. \tag{A.24}$$

Substituting $u = \sqrt{2k_BT/M}$:

$$\Delta\omega_D = \frac{2\omega_0}{c}\sqrt{\ln 2}\sqrt{\frac{2k_BT}{M}}. \tag{A.25}$$

Hence, the Doppler width scales as

$$\Delta\omega_D \propto \sqrt{\frac{T}{M}}. \tag{A.26}$$

Thus, Doppler broadening increases with temperature and decreases with atomic mass.